

Self-organization in planar magnetron microdischarge plasmas

Cite as: Appl. Phys. Lett. **106**, 254104 (2015); <https://doi.org/10.1063/1.4922898>

Submitted: 10 May 2015 . Accepted: 12 June 2015 . Published Online: 25 June 2015

Tsuyohito Ito, Christopher V. Young , and Mark A. Cappelli



View Online



Export Citation



CrossMark

ARTICLES YOU MAY BE INTERESTED IN

[Tutorial: Physics and modeling of Hall thrusters](#)

Journal of Applied Physics **121**, 011101 (2017); <https://doi.org/10.1063/1.4972269>

[Nonlinear structures and anomalous transport in partially magnetized \$E \times B\$ plasmas](#)

Physics of Plasmas **25**, 011608 (2018); <https://doi.org/10.1063/1.5001206>

[E×B electron drift instability in Hall thrusters: Particle-in-cell simulations vs. theory](#)

Physics of Plasmas **25**, 061204 (2018); <https://doi.org/10.1063/1.5017033>

Lock-in Amplifiers
up to 600 MHz



Self-organization in planar magnetron microdischarge plasmas

Tsuyohito Ito,¹ Christopher V. Young,² and Mark A. Cappelli^{2,a)}

¹Center for Atomic and Molecular Technologies, Graduate School of Engineering, Osaka University, 2-1 Yamadaoka, Suita, Osaka 565-0871, Japan

²Stanford Plasma Physics Laboratory, 452 Escondido Mall, Bldg. 520-257, Stanford, California 94305, USA

(Received 10 May 2015; accepted 12 June 2015; published online 25 June 2015)

Evidence is presented of rotating azimuthal wave structures in a planar magnetron microdischarge operating at 150 mTorr in argon. Plasma emission captured using a high frame rate camera reveals waves of azimuthal modes $m=3-5$ propagating in the $-\vec{E} \times \vec{B}$ direction. The dominant stable mode structure depends on discharge voltage. The negative drift direction is attributed to a local field reversal arising from strong density gradients that drive excess ions towards the anode. The transition between modes is shown to be consistent with models of gradient drift-wave dispersion in the presence of such a field reversal when the fluid representation includes ambipolar diffusion along the direction parallel to the magnetic field. © 2015 AIP Publishing LLC.

[<http://dx.doi.org/10.1063/1.4922898>]

Applications of low pressure discharge in crossed electric and magnetic fields date as far back as 1936 when Penning proposed their use for measuring pressure.¹ Since then, $\vec{E} \times \vec{B}$ devices such as magnetron, inverted magnetron, and Hall discharges have played important roles in many technologies. Inverted magnetrons have extended the range of pressure measurements beyond that of the first “Penning” gauges.² Planar magnetron discharges operating in direct current (DC), radio frequency,³ and high power pulsed modes⁴ are widely used as sputter deposition sources. Hall thrusters^{5,6} have seen increased use in space propulsion and variants have been used as ion sources for materials processing.⁷

Despite the commercial successes of these discharges, aspects of their operation, such as how electrons are heated⁸ and migrate across the magnetic field⁹ are not well understood. Prevailing theories link these processes to plasma fluctuations. At very low pressures (<1 Pa), fluctuations have been attributed to sheath (“diocatron”) instabilities,¹⁰⁻¹² driven unstable by shearing in the azimuthal electron current.¹³ At higher pressure and high densities, as in high power impulse magnetron sputtering (HiPIMS) sources,¹⁴⁻¹⁶ the instabilities are driven by ionization.^{8,14} In some cases, the instabilities in these devices exhibit spatial and temporal coherence characteristic of self-organization.¹⁷⁻¹⁹ In higher pressure discharges with lower current densities than in HiPIMS, such as many DC planar magnetron sources and stationary plasma thrusters, fluctuations have been attributed to drift waves²⁰ that are similar to those seen in devices without externally imposed electric fields, E_0 (e.g., Q-machines).²¹ The drift waves are affected by the electric field-driven drift velocity, v_E , resulting from the imposed magnetic field, B_0 : $v_E = E_0/B_0$. These drift waves are rendered unstable by gradients in the plasma density or the magnetic field²² and further destabilized by the diffusion of plasma along the magnetic field.²³

We have reported strong coherence and self-organization in a magnetron microdischarge that operates continuously with a constant applied voltage.^{24,25} Variations were developed for use as micro-ion sources²⁶ and micro-Hall thrusters.²⁷ The observed instabilities propagate in the $-\vec{E} \times \vec{B}$ direction, in contrast to what has been reported in HiPIMS sources,^{14,28,29} suggesting that the mechanisms behind the instabilities in these two operating regimes are associated with different physical processes. It was shown recently³⁰ that coherent structures in HiPIMS reverse direction during a phase in the pulse cycle when the current falls below a threshold value, further suggesting a change in the governing physics. The quasi-steady current density in our DC microdischarge appears to be anomalous on average, i.e., cannot be accounted for by classical electron scattering with the background gas. We suspect that this is driven by the low-frequency instabilities underlying the observed self-organization.²⁴ As shown below, these instabilities exhibit interesting mode transitions and dependencies on the applied potential.

Because of the relatively high pressure ($\sim 10-20$ Pa) and plasma densities ($\sim 10^{13}$ cm⁻³), the plasma is quasi-neutral. The millimeter scale produces strong plasma and magnetic field gradients ($\sim 10^{14}$ cm⁻⁴ and 5 T/cm, respectively), so we interpret our results using models for gradient-driven drift instabilities originally developed to explain low frequency waves seen in Hall thrusters.^{22,31} We extend the model of Ref. 31 to include transport along the magnetic field, expanding the domain of instability. The model results are in good agreement with the observed experimental behavior: waves propagate in the $-\vec{E} \times \vec{B}$ direction with frequencies between 100 and 500 kHz exhibiting strong dependency on the local electric field. To obtain this agreement, we must assume a field reversal within the discharge, which is plausible when density gradients are strong and diffusion drives more anode-bound electrons than demanded by the external circuit. Field reversals are commonly seen in hybrid simulations of Hall thrusters^{32,33} and one was recently hypothesized to explain electron heating and unsteady behavior⁸ and enhanced ion back-flow³⁴ in HiPIMS sources.

^{a)}Electronic mail: cap@stanford.edu

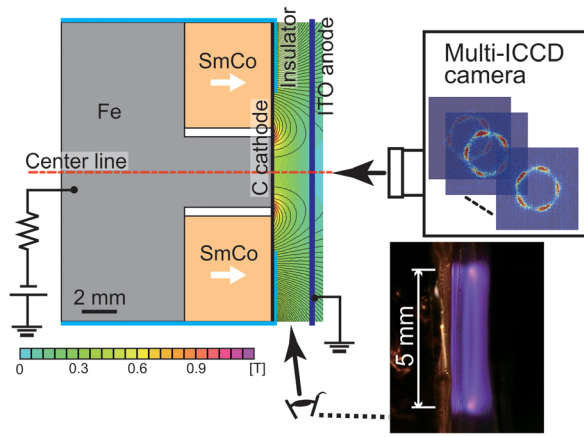


FIG. 1. Schematic of the discharge geometry, magnetic field, and optical diagnostics.

A schematic of the experiment appears in Fig. 1. Plasma forms between a $120\ \mu\text{m}$ graphite cathode and a transparent indium tin oxide (ITO) anode, providing direct optical access. The lower right spectrally and temporally integrated photograph in Fig. 1, taken obliquely from the side, demonstrates the toroidal structure. A high framing rate camera captures time-varying axial plasma emission through the ITO anode, as shown at top right (see also Fig. 2). In this work, the variable discharge gap is either 2 mm or 2.8 mm, with 20 Pa (0.15 Torr) argon pressure.

A 17 mm diameter samarium-cobalt (SmCo) permanent ring magnet with an iron core generates the magnetic field topology, simulated with a finite element solver³⁵ and shown overlaid on the 2 mm discharge gap in Fig. 1. The toroidal field is uniform in the azimuthal direction but varies strongly

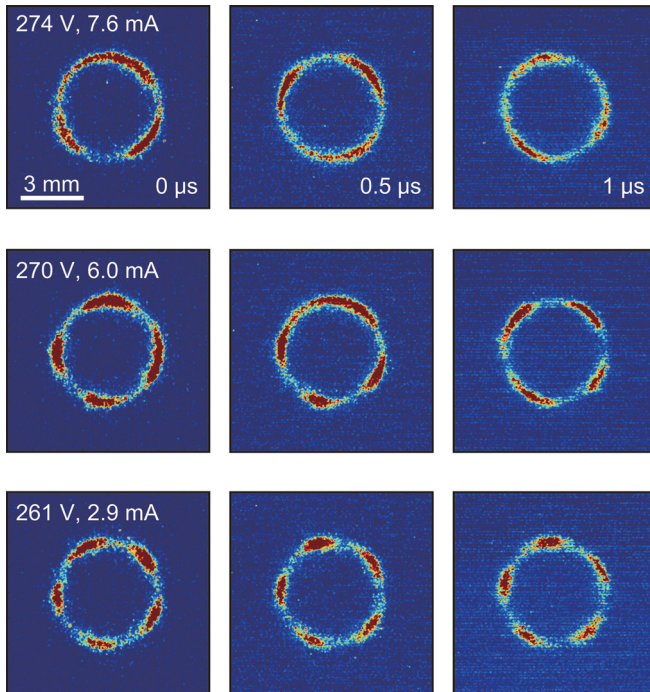


FIG. 2. Three sequences of images of the 150 mTorr argon plasma with a 2 mm gap captured with a high speed camera. Waves ($m=3-5$) are propagating clockwise, opposite the $\vec{E} \times \vec{B}$ direction. The images are normalized to the strongest intensity in each frame. Error in scale between figures might be up to 5%.

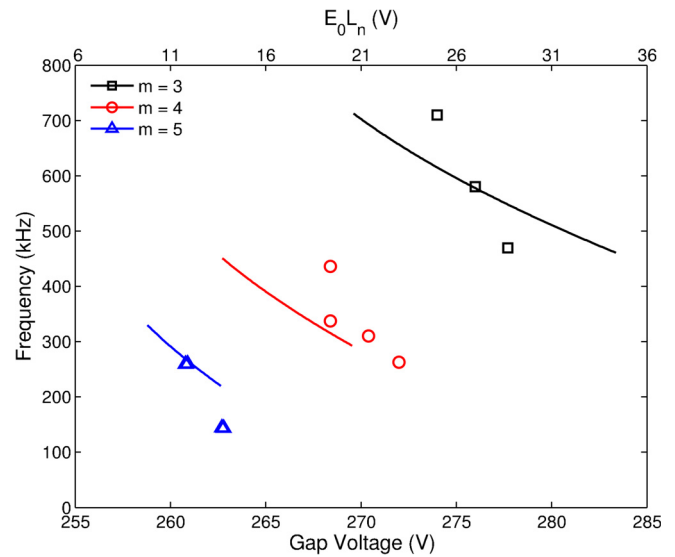


FIG. 3. A comparison of the measured mode frequencies (symbols) to those predicted by the analysis (lines) as a function of experimental discharge voltage (lower abscissa) and modeled voltage “hump” $E_0 L_n$ due to field reversal (upper abscissa). The scales are matched assuming a 12 V voltage hump when the discharge voltage is 261 V.

(radially in \hat{r} , and axially in \hat{z}) between the cathode and anode. The maximum field at the cathode is approximately 1 T, falling to ~ 0.5 T halfway between the electrodes. This produces an axial field gradient $\partial B_0 / \partial z \approx 0.5$ T/mm, or a characteristic field decay length $L_B = (\partial \ln B_0 / \partial z)^{-1} \approx 0.5$ mm. Gradients along the radial direction are comparable to the axial gradients, a condition which holds in the presence of a discharge current density J ($\sim 10^3$ A/m²) since $\mu_0 J L_B / B_0 \ll 1$.

At a field of about 1 T, 10 eV argon ions are weakly magnetized, with a gyroradius of ~ 3 mm—larger than the electrode spacing. The electrons are strongly magnetized and confined to tight gyro-orbits near regions of ionization while diffusing along the field lines between the inner and outer cusps of the toroid. Electron diffusion along directions parallel to the field is tied to that of the ions (ambipolar diffusion), establishing a parallel component to the electric field.

Images are obtained through the anode with a high framing rate camera (Cordin, Model 222C-16UV) consisting of eight individual intensified charge coupled device (ICCD) detectors that can be gated relative to each other by approximately 10 ns (an effective framing rate of ~ 100 MHz). Each detector can acquire two photographs within as low as 3 μs , leading to an effective framing rate of ~ 2.7 MHz when acquiring all 16 frames.

We note that discharge current-voltage (I - V) characteristics are relatively insensitive to the gap length and show only small fluctuations ($\sim 1\%$) on top of the DC component, despite strong coherent azimuthal fluctuations in the recorded plasma emission (Fig. 2). This suggests that while the observed fluctuations may play a role in establishing the conductance of the discharge, they do not seem to affect the steady state operating condition.

Figure 2 shows sequences of consecutive images of unfiltered emission from the discharge, operating at 274 V and 7.6 mA (top row), 270 V and 6.0 mA (middle row), and 261 V and 2.9 mA (bottom row). The gap length is 2 mm and

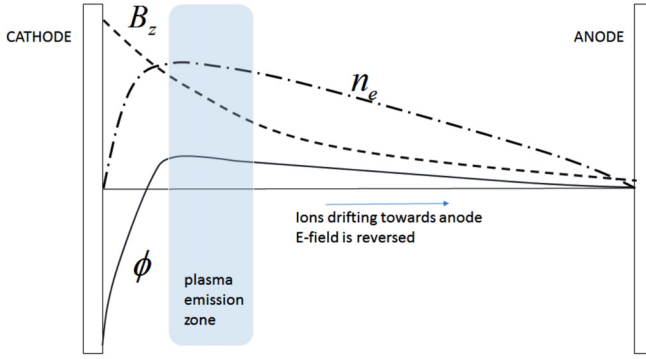


FIG. 4. Illustration of the assumed plasma structure within the discharge for the gradient-drift model.

the images are acquired $0.5 \mu\text{s}$ apart. The single frame integration time (gate width) is $0.75 \mu\text{s}$ for the 274 V and 270 V cases, and $1 \mu\text{s}$ for the 261 V case. These integration times provide favorable signal to noise characteristics but do tend to smear the azimuthal structures depicted. Each image in Fig. 2 spans a field of $9.6 \text{ mm} \times 9.6 \text{ mm}$, or 1.5×10^5 pixels. The images are smoothed over the 8 nearest neighboring pixels to remove pixel-to-pixel variations in sensitivity. We observe three mode numbers in the images, ranging from $m = 3$ to 5, and have confirmed the mode number and propagation direction by reducing the exposure time to $0.1 \mu\text{s}$ (not shown). The mode number decreases with increasing discharge voltage and the structures propagate in the $-\vec{E} \times \vec{B}$ direction (clockwise in the images; \vec{E} is defined as the imposed field).

The frequencies of the waves extracted from the high-speed images are shown as symbols in Fig. 3. For fluctuations with the same azimuthal wavelength (mode number), the frequency decreases with increasing voltage. As the voltage increases beyond some critical value, a mode transition to longer wavelengths occurs and the frequency abruptly increases. The simultaneous jump in frequency and wavelength (reduced mode number, m) indicates a substantial increase in the wave's phase velocity.

We interpret these data using gradient-driven drift theories proposed in Refs. 22 and 31. The analysis considers a two-dimensional, two-fluid model where the ions are non-magnetized and electrons are strongly magnetized. We unfold the annular geometry onto a Cartesian coordinate system with an electric field E_0 oriented along the discharge axis (\hat{x} -direction, positive from anode to cathode), and a magnetic field B_0 taken primarily along the \hat{z} -direction (radially outwards). The background plasma (assumed uniform in the \hat{y} -direction) contains plasma density (n_0) and magnetic field gradients along the \hat{x} -direction, as illustrated qualitatively in Fig. 4. We presume that the strongest ionization and emission occur just beyond the cathode fall, where plasma density gradients near the anode produce a field reversal, $E_0 < 0$, driving ions towards the anode. An analogous reverse ion migration was measured by laser induced fluorescence in the near anode region of Hall thrusters.⁹

As described in Refs. 22 and 31, linearized species continuity and momentum equations for the plasma constituent number densities and velocities are subject to Fourier perturbations to describe the dispersion conditions for wave

propagation. The quiescent plasma electrons experience diamagnetic (isothermal) and $\vec{E} \times \vec{B}$ drifts, respectively,

$$\vec{v}_{eD} \approx -\frac{kT_e}{eB_0} \frac{1}{n_0} \frac{dn_0}{dx} \hat{y} = -\frac{kT_e}{eB_0 L_n} \hat{y}, \quad (1)$$

$$\vec{v}_{eE \times B} \approx -\frac{E_0}{B_0} \hat{y}. \quad (2)$$

Here, e is the electron charge, k is Boltzmann's constant, and T_e is the electron temperature. When substituted into the electron continuity equation, these drifts result in an equation for the evolution of the electron density that accounts for magnetic field compressibility²³

$$\frac{\partial n_e}{\partial t} + \vec{v}_{eD} \cdot \nabla n_e - 2n_e (\vec{v}_{eD} + \vec{v}_{eE \times B}) \cdot \nabla \ln \vec{B}_0 + \frac{\partial}{\partial z} (n_e v_{ez}) = 0. \quad (3)$$

This equation differs from that in Ref. 31 by the last term, which describes diffusion along the magnetic field lines. As in Ref. 23, we assume electron/ion collisionality along the B -parallel ($\sim \hat{z}$ -direction) only. Invoking quasi-neutrality, the electrons and ions diffuse together with a \hat{z} -directed flux, $\Gamma_{e,iz} = D_A \partial n_e / \partial z$. Here, $D_A = kT_e / m_i \nu_i$ is the ambipolar diffusion coefficient, m_i is the ion mass, and ν_i is the ion momentum transfer collision frequency estimated from the ion drift velocities compiled by Hornbeck.³⁶

By assuming small perturbations of the form $\xi = \tilde{\xi} \exp [i(k_x x + k_y y + k_z z - \omega t)]$, the linearized equations give rise to the following dispersion relation for the frequency (ω) dependence on wavenumber components perpendicular to B_0 (k_\perp) and parallel to E_0 (k_x)

$$\omega^2 - \left(2k_x v_{i0} + \frac{k_\perp^2 c_s^2}{\omega^* - \omega_D} \right) \omega + k_x^2 v_{i0}^2 + \frac{k_\perp^2 c_s^2 (\omega_0 + \omega_D)}{\omega^* - \omega_D} - i \frac{k_\perp^2 c_s^2 \nu_c}{\omega^* - \omega_D} = 0. \quad (4)$$

Here, $c_s = \sqrt{kT_e / m_i}$ is the ion acoustic speed, v_{i0} is the ion drift velocity due to the external electric field, $\nu_c = k_z^2 D_A$ is a collisional dissipation rate, $\omega^* = k_y v_{eD}$, $\omega_0 = k_y v_{E \times B}$, and $\omega_D = -(2kT_e / eB_0 L_B) \hat{y}$.

In the absence of the diffusive term, the dispersion will have identical characteristics to that derived in Ref. 31, and, with E_0 (and v_{i0}) < 0 , the region of instability has a distinct long wavelength cutoff that depends on background plasma conditions. We calculate the predicted growth rate of the unstable branch (imaginary component of the dispersion solution assuming real wavenumbers) using plausible experimental conditions— $E_0 = -11.6 \text{ kV/m}$, $L_n = 2 \text{ mm}$ ($E_0 L_n = -23.1 \text{ V}$), $L_B = 0.5 \text{ mm}$, $kT_e = 3.1 \text{ eV}$, $B_0 = 0.6 \text{ T}$, $k_x = 7.0 \text{ mm}^{-1}$, $k_z = 2.5 \text{ mm}^{-1}$, and $v_{i0} = -933 \text{ m/s}$ —and plot the result as the solid line in Fig. 5(a). The maximum growth rate is somewhere between $m = 3$ and $m = 4$, and increasing the electric field shifts the cutoff and peak towards longer wavelengths. Including the diffusive term (using $\nu_i = 5 \times 10^7 \text{ s}^{-1}$) modifies the growth rate, extending the region of instability beyond the original cutoff (see the dotted line in Fig. 5(a)). As the discharge voltage increases, we expect an active $m = 4$ mode until the peak growth rate passes a critical value, triggering a

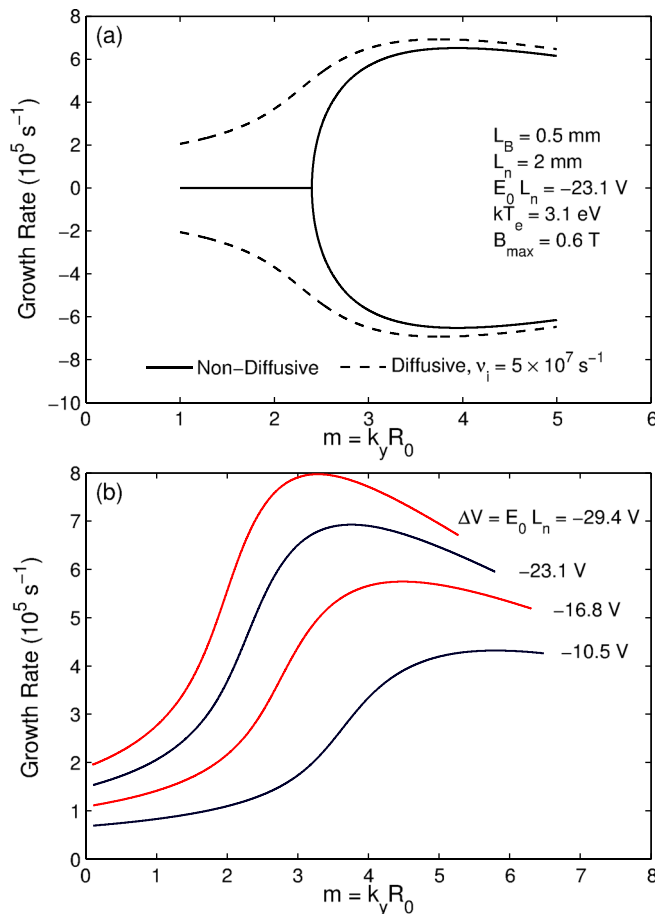


FIG. 5. (a) Growth rate of the instability versus mode number for the diffusive (dashed) and non-diffusive (solid) cases. (b) Growth rate variation with mode number computed for a range of values of the voltage “hump.”

mode transition to $m=3$. The variation in the peak growth rate with electric field is shown in Fig. 5(b). When increasing the field, we assume a simple scaling that $kT_e \sim E_0$ and $v_{i0} \sim E_0^{1/2}$.

The real component of the frequencies of the unstable root tends to decrease with increased electric field while within the range of instability for any single mode. As illustrated by the solid lines in Fig. 3, once a new mode is preferred (higher m for voltage increases), a jump in frequency is predicted. To compare the experiments with the model, we have assumed that a 12 V voltage “hump” ($E_0 L_n$) is generated when the discharge voltage is 261 V. No other adjustments are made to the predicted dispersion. The values chosen for various plasma parameters are the same as those listed above and used in Fig. 5. Agreement with experiments is good, considering the uncertainties in the properties used as base conditions. A model tested without including the diffusive terms in Eqs. (3) and (4) fails to achieve such an agreement.

The microdischarge studied here is an excellent test bed for understanding gradient-driven instabilities in cross-field discharges. The observed mode transitions are distinct, coherent, and reproducible. A simple theory for the dispersion of these gradient-driven drift waves seems to describe these instabilities quite well. The success of the model rests heavily on the presumption of a field reversal, generating a

voltage “hump” that drives a reverse (anode-directed) ion flow, and future experiments will seek confirmation of such a structure.

This study was supported by the Air Force Office for Scientific Research. C.Y. acknowledges support from the DOE NNSA Stewardship Science Graduate Fellowship under Contract No. DE-FC52-08NA28752 and the Stanford Graduate Fellowship.

¹F. M. Penning, *Physica* **3**, 873 (1936).

²A. Beck and A. Brisbane, *Vacuum* **2**, 137 (1952).

³R. K. Waits, *J. Vac. Sci. Technol.* **15**, 179 (1978).

⁴J. Gudmundsson, N. Brenning, D. Lundin, and U. Helmersson, *J. Vac. Sci. Technol., A* **30**, 030801 (2012).

⁵H. R. Kaufman, *AIAA J.* **23**, 78 (1985).

⁶V. Zhurin, H. Kaufman, and R. Robinson, *Plasma Sources Sci. Technol.* **8**, R1 (1999).

⁷V. V. Zhurin, “Hall-Current Ion Sources,” in *Industrial Ion Sources: Broadbeam Gridless Ion Source Technology* (Wiley-VCH Verlag GmbH & Co. KGaA, 2012).

⁸A. Anders, *Appl. Phys. Lett.* **105**, 244104 (2014).

⁹N. B. Meezan, W. A. Hargus, Jr., and M. A. Cappelli, *Phys. Rev. E* **63**, 026410 (2001).

¹⁰R. Levy, *Phys. Fluids* **8**, 1288 (1965).

¹¹P. Redhead, *Vacuum* **38**, 901 (1988).

¹²J.-P. Boeuf, *Front. Phys.* **2**, 74 (2014).

¹³S. N. Abolmasov, S. Samukawa, and A. A. Bizyukov, *Phys. Plasmas* **14**, 093501 (2007).

¹⁴A. Kozyrev, N. Sochugov, K. Oskomov, A. Zakharov, and A. Odivanova, *Plasma Phys. Rep.* **37**, 621 (2011).

¹⁵J. Winter, A. Hecimovic, T. De los Arcos, M. Böke, and V. Schulz-von der Gathen, *J. Phys. D: Appl. Phys.* **46**, 084007 (2013).

¹⁶M. Panjan, R. Franz, and A. Anders, *Plasma Sources Sci. Technol.* **23**, 025007 (2014).

¹⁷A. Ehasarian, A. Hecimovic, T. De Los Arcos, R. New, V. Schulz-Von Der Gathen, M. Böke, and J. Winter, *Appl. Phys. Lett.* **100**, 114101 (2012).

¹⁸J. Andersson, P. Ni, and A. Anders, *Appl. Phys. Lett.* **103**, 054104 (2013).

¹⁹A. Anders, P. Ni, and J. Andersson, *IEEE Trans. Plasma Sci.* **42**, 2578 (2014).

²⁰W. Horton, *Rev. Mod. Phys.* **71**, 735 (1999).

²¹T. Chu, B. Coppi, H. Hendel, and F. Perkins, *Phys. Fluids* **12**, 203 (1969).

²²A. Kapulkin and M. M. Guelman, *IEEE Trans. Plasma Sci.* **36**, 2082 (2008).

²³J. C. Perez, W. Horton, K. Gentle, W. Rowan, K. Lee, and R. B. Dahlburg, *Phys. Plasmas* **13**, 032101 (2006).

²⁴T. Ito and M. A. Cappelli, *IEEE Trans. Plasma Sci.* **36**, 1228 (2008).

²⁵T. Ito and M. A. Cappelli, *Appl. Phys. Lett.* **94**, 211501 (2009).

²⁶T. Ito and M. A. Cappelli, *Appl. Phys. Lett.* **89**, 061501 (2006).

²⁷T. Ito, N. Gascon, W. S. Crawford, and M. A. Cappelli, *J. Propul. Power* **23**, 1068 (2007).

²⁸A. Anders, P. Ni, and A. Rauch, *J. Appl. Phys.* **111**, 053304 (2012).

²⁹T. de los Arcos, V. Layes, Y. A. Gonzalvo, V. Schulz-von der Gathen, A. Hecimovic, and J. Winter, *J. Phys. D: Appl. Phys.* **46**, 335201 (2013).

³⁰Y. Yang, J. Liu, L. Liu, and A. Anders, *Appl. Phys. Lett.* **105**, 254101 (2014).

³¹W. Frias, A. I. Smolyakov, I. D. Kaganovich, and Y. Raitses, *Phys. Plasmas* **19**, 072112 (2012).

³²M. K. Scharfe, N. Gascon, M. A. Cappelli, and E. Fernandez, *Phys. Plasmas* **13**, 083505 (2006).

³³F. Parra, E. Ahedo, J. Fife, and M. Martinez-Sanchez, *J. Appl. Phys.* **100**, 023304 (2006).

³⁴N. Brenning, C. Huo, D. Lundin, M. A. Raadu, C. Vitelaru, G. Stancu, T. Minea, and U. Helmersson, *Plasma Sources Sci. Technol.* **21**, 025005 (2012).

³⁵D. Meeker, see <http://www.femm.info/wiki/HomePage> for finite element method magnetics, 2011.

³⁶J. A. Hornbeck and J. Molnar, *Phys. Rev.* **84**, 621 (1951).